In Situ Silver-based Electrochemical Bioreactor In Vivo

Yong Huang
Guangxi Medical University/National Center for International Research of Biotheranostics
Liping Zhong
Guangxi Medical University/National Center for International Research of Biotheranostics
Zhiming Deng
Guangxi Medical University/National Center for International Research of Bio-targeting Theranostics
Pan Wu
Guangxi Medical University/National Center for International Research of Bio-targeting Theranostics
Jian He
National Center for International Research of Biological Targeting Diagnosis and Therapy
Zhihao Bai
National Center for International Research of Biological Targeting Diagnosis and Therapy
Yi Zhong
National Center for International Research of Biological Targeting Diagnosis and Therapy
Hongmei Hongmei Peng
National Center for International Research of Biological Targeting Diagnosis and Therapy
Kun Zhang
Tongji University School of Medicine https://orcid.org/0000-0002-6971-1164
Xing-Jie Liang
National Center for Nanoscience and Technology https://orcid.org/0000-0002-4793-1705
Yongxiang Zhao (yongxiang_zhao@126.com)
Guangxi Medical University/National Center for International Research of Bio-targeting Theranostics

Article

Keywords: Silver-based electrochemical oncolytic bioreactor (SEOB), Intratumoral silver-based nanosynthetic prodrug, Primate biosafety, Aptamer targeting

Posted Date: November 16th, 2020

DOI: https://doi.org/10.21203/rs.3.rs-103588/v1

Abstract

In this study we show for the first time that a reduced graphene oxide (rGO) carrier has a 15-fold higher catalysis rate than graphene oxide (GO) in Ag^+ reduction. Based on this, we constructed a tumor microenvironment-enabled *in situ* silver-based electrochemical oncolytic bioreactor (SEOB) which unlocked an Ag^+ prodrug to generate silver nanoparticles and inhibited the growth of various tumors. In this bioreactor system, intratumoral H_2O_2 acted as the reductant and the rGO carrier acted as the catalyst. Chelation of aptamers to this prodrug increased the production of silver nanoparticles by tumor cells, especially in the presence of Vitamin C, which broke down in tumor cells to supply massive amounts of H_2O_2. Consequently, highly efficient silver nanoparticle-induced apoptosis was observed in HepG2 and A549 cells *in vitro* and in HepG2- and A549-derived tumors *in vivo.* The apoptosis was associated with ROS-induced changes in mitochondrial membrane potential and DNA damage. The specific aptamer targeting and intratumoral silver nanoparticle production guaranteed excellent biosafety, with no damage to normal cells, because the Ag^+ prodrug was specifically unlocked in tumors. More significantly, there was no evident tissue damage in monkeys, which greatly increases the clinical translation potential of the SEOB system.

Introduction

Since the concept of nanomedicine came into existence[1-3], various nanomaterials have been developed to execute diagnosis or treatment of malignant tumors[4-8]. However, the unsatisfactory delivery efficiency into tumors and universal distribution across all organs remain unresolved and intractable challenges even in the presence of active targeting. Enlightened by a microbial medicine factory[9,10], a concept has emerged in which a biological body can act as a bioreactor for *in situ* production of functional nanoagents *via* chemical reaction or physical assembly of injected precursors. The specific species and microenvironment within the biological body can act as catalysts, stimuli or reactants[11,12]. This biosynthesis technology holds great potential for overcoming the systemic toxicity and low delivery efficiency that are associated with current drug delivery systems[13]. Nevertheless, this technology is still at its infancy, especially for biosynthesis of anti-tumor nanomaterials. Herein, inspired by intriguing reports highlighting H_2O_2 as a reductant[14,15], we developed a tumor microenvironment-enabled *in situ* silver-based electrochemical oncolytic bioreactor (SEOB) to unlock an Ag^+ prodrug, which establishes the intratumoral silver-based nanosynthetic medicine. The underlying principle of the SEOB theory is illustrated in **Fig. 1a**.

In this unprecedented SEOB theory, intratumoral H_2O_2 can facilitate *in situ* reduction of an Ag^+-DNA conjugate prodrug loaded in reduced graphene oxide (rGO) nanosheets. This leads to intratumoral production of silver nanoparticles, which are regarded as excellent anti-tumor agents due to their ability to induce the production of reactive oxygen species (ROS)[16,17]. rGO is a well-accepted drug carrier[18-20], which can accommodate Ag^+-DNA. In addition, rGO features few oxygen-containing groups on its

surface, and therefore benefits rapid electron transfer[21-23], which enables the rapid reduction of Ag^+ by H_2O_2 in the tumor. Notably, DNA-Ag^+ conjugate prodrug is obtained *via* the coordination interaction, wherein DNA is highlighted to stabilize Ag^+, manipulate Ag^+ loading content, avoid self-driven Ag+ nucleation and growth, improve biosafety via reducing Ag+ leakage and supply rich binding sites for the subsequent chitosan (CS) coating.

To improve the accumulation of the Ag^+ prodrug-carrying bioreactor in the tumor, rGO was coated with CS, then further conjugated with aptamers (Apts) targeting proteins that are specifically overexpressed in tumor cells. Two Apts were used, *i.e.*, AS1411 and endoglin (END), which target nucleolin and endoglin, respectively[24]. Thus, we obtained two Ag^+ prodrug-carrying bioreactors (represented as Apt-CS/rGO/Ag^+-DNA), namely END-CS/rGO/Ag^+-DNA and AS1411-CS/rGO/Ag^+-DNA (**Fig. 1b**). Our strategy is designed to deliver more Ag^+-DNA conjugates into tumors, which then generate intratumoral silver nanoparticles and further facilitate silver nanoparticle-mediated anti-tumor effects. It has been shown that that Vitamin C (VitC) can specifically kill tumor cells when it breaks down to produce H_2O_2[25-29]. Tumor cells have low catalase activity compared to normal cells, and cannot efficiently clear H_2O_2. Therefore, exogenously supplemented VitC is anticipated to cause massive production of H_2O_2 in tumor cells, which acts as a reductant to produce more silver nanoparticles, thus delivering highly efficient anti-tumor activity (**Fig. 1a**). More impressively, the aptamer-mediated tumor targeting and specific generation of intratumoral silver nanoparticles guarantees the excellent biosafety of this bioreactor system. The SEOB causes no evident damage to the main organs of cynomolgus monkeys, which indicates that it is suitable for clinical translation.

Results

VitC-enhanced H_2O_2 reduction assay

We firstly investigated whether H_2O_2 can act as the reductant, because this is an essential prerequisite to fulfil the function of the SEOB. Herein, VitC was used to increase H_2O_2 production in HepG2 tumor cells, since several studies have reported VitC-derived H_2O_2 elevation in tumor cells [25-27]. When we treated HepG2 cells with Ag^{2+} alone, we observed black silver deposits due to the pre-existing H_2O_2 in the cells (Supplementary **Fig. S1**). However, many more silver deposits were observed when VitC was added prior to or after Ag^+ to stimulate the production of H_2O_2. This confirms that H_2O_2 can indeed behave as the reductant to reduce Ag^+ into silver nanoparticles. The level of silver nanoparticles increases as either the Ag^+ concentration or the incubation time escalates, accompanied by more silver-induced HepG2 apoptosis (Supplementary **Figs S2 and S3**). To test the ability of VitC to induce H_2O_2 production *in vivo*, we used mice bearing HepG2-derived tumors. We injected mice intratumorally or intravenously with VitC, then monitored changes in the electrical current in the tumor, which reflect the H_2O_2 level. Significantly increased current signals, representing increased H_2O_2 levels only at the tumor site occurred after intratumoral or intravenous injection of VitC (**Fig. 1c-e**). This implies that VitC-derived H_2O_2 can reduce

the Ag^+-based prodrug *in vivo*. However, silver deposition induced by H_2O_2 alone is inadequate due to the low reduction efficiency. To address this, rGO was used as the catalyst.

Analysis of the catalytic activity of rGO

Despite sharing similar structures with grapheme oxide (GO) (Supplementary **Fig. S4**), rGO is preferred to promote electron separation and H_2O_2 disproportionation due to its much higher catalytic activity[21-23]. Compared to GO, rGO allows rapid electron transfer and favors free Ag^+ deposition, as evidenced by the larger silver stripping current, shorter stable response time and higher H_2O_2 disproportionation current in various anodic stripping voltammetry (ASV) tests (**Fig. 1f-h**). Based on these extraordinary features, we selected rGO to accelerate Ag^+ reduction by H_2O_2. Furthermore, silver deposition from an Ag^+-DNA conjugate was explored *via* ASV testing. The results showed that the successful capture of Ag^+ by DNA can concentrate Ag^+ and generate the strongest silver nanoparticle-derived current signal (**Fig. 1i**). This implies that Ag^+ chelated to DNA was efficiently reduced by H_2O_2 to augment the silver deposition. Therefore, it is reasonable to expect that the Apt-CS/rGO/Ag^+-DNA prodrug will rapidly and efficiently produce silver nanoparticles in the presence of rGO catalyst. To understand why rGO can achieve such a high catalytic activity for silver deposition, Raman, Fourier transform infrared (FT-IR) and X-ray photoelectron spectroscopy (XPS) characterizations were carried out. Compared to GO, rGO had a higher D/G ratio and fewer oxygen-containing functional groups (Supplementary **Fig. S5**). The decreased oxygen content in rGO means that more sp^2 hybrid orbitals are available for accommodating electrons. In this regard, rGO can undoubtedly increase electron transfer from disproportionated H_2O_2 to Ag^+, thus favoring catalytic reduction of Ag^+ and deposition of silver nanoparticles.

Synthesis of a bioreactor carrying the Ag^+ prodrug

The decreased level of oxygen-containing functional groups in rGO facilitates π-π conjugation, which will enhance the binding affinity between rGO and Ag^+-conjugated DNA chains (Ag^+-DNA) and enable rGO stacking (**Fig. 2a**). When the rGO carrier is chelated with Ag^+-DNA conjugates, coated with CS and modified with AS1411 aptamers, the structure of the carrier is not changed (**Fig. 2b**). This suggests that AS1411-CS/rGO/Ag^+-DNA will retain the rGO-catalyzed silver deposition property. The presence of uniformly distributed Ag and P elements demonstrates the successful chelation of Ag^+-DNA conjugates onto rGO in AS1411-CS/rGO/Ag^+-DNA (**Fig. 2c-e**). New FT-IR characteristic peaks and changes in the zeta potential also demonstrate the successful synthesis of AS1411-CS/rGO/Ag^+-DNA and its intermediate products in sequence (**Fig. 2f,g**). During the modification process, the particle size remains approximately constant (Supplementary **Fig. S6a**).

Aptamer-mediated targeting assay *in vitro*

AS1411 specifically targets nucleolin, which is overexpressed by many tumors[30-32]. Therefore, we investigated the internalization of AS1411-CS/rGO/Ag^+-DNA into HepG2 cells, which overexpress

nucleolin. Direct analyses by laser confocal scanning microscopy (LCSM) and flow cytometry were firstly performed. A random sequence (RS) incapable of tumor targeting was used instead of AS1411 to synthesize the control nanosystem (*i.e.*, RS-CS/rGO/Ag^+-DNA). Furthermore, the L02 cell line, which features low nucleolin expression, was used as another comparison. The results clearly showed that more AS1411-CS/rGO/Ag^+-DNA than RS-CS/rGO/Ag^+-DNA entered the HepG2 cells, and both systems failed to enter L02 cells (**Fig. 2h**). This result sufficiently validates the specific targeting of AS1411 to nucleolin-overexpressing HepG2 cells. Flow cytometry data also confirms that there is more accumulation of AS1411-CS/rGO/Ag^+-DNA in HepG2 cells than RS-CS/rGO/Ag^+-DNA (Supplementary **Fig. S7**).

SEOB unlocks the Ag^+ prodrug for silver deposition and anti-tumor activity

Contributed by AS1411 targeting-enhanced AS1411-CS/rGO/Ag^+-DNA accumulation, VitC-enhanced H_2O_2 production and rGO-catalyzed silver deposition, AS1411-CS/rGO/Ag^+-DNA+VitC group exerts the most robust killing ability against HepG2 cells. (**Fig. 2i**) This phenomenon attributed to that silver nanoparticles birth in the AS1411-CS/rGO/Ag^+-DNA+VitC group gave birth to more oxidative stress for altering or preventing cell cycle progression. However, the targeting ability of AS1411 determines AS1411-CS/rGO/Ag^+-DNA failed to induce evident injures to normal liver cells with low nucleolin expression (*e.g.*, L02) (**Fig. 2k**). Intriguingly, VitC-enhanced H_2O_2 production alone does not kill HepG2 and L02 cells (**Fig. 2j**), and few AS1411-CS/rGO/Ag^+-DNA and RS-CS/rGO/Ag^+-DNA nanoparticles accumulate in L02 cells because these systems are not specifically targeted to L02 (**Fig. 2k,l**). These impressive results (*i.e.* assessment of the levels of silver deposition and cell apoptosis) indirectly validate the targeting ability of AS1411. More significantly, laser confocal scanning microscopy (LCSM) observations of HepG2 cells after live/dead co-staining also demonstrate that AS1411-CS/rGO/Ag^+-DNA+VitC induces the most cell apoptosis and results in the lowest cell density (**Fig. 2m**).

In-depth exploration of the anti-tumor effect of AS1411-CS/rGO/Ag^+-DNA+VitC was carried out *via* monitoring the variation of mitochondrial membrane potential. The strongest green fluorescence of JC-1 monomers was observed in AS1411-CS/rGO/Ag^+-DNA+VitC-treated HepG2 cells (**Fig. 3a**). This reflects the significantly decreased membrane potential in these cells, and suggests a high level of apoptosis. In contrast, the negligible level of green fluorescence in L02 cells indicates no change in membrane potential and no L02 apoptosis, which can be attributed to poor accumulation of AS1411-CS/rGO/Ag^+-DNA in L02 cells (**Fig. 3b**). These results adequately demonstrate that AS1411-CS/rGO/Ag^+-DNA in the presence of VitC can produce the most silver deposits, which triggers the greatest anti-tumor activity. Quantitative data also confirms that although VitC-enhanced H_2O_2 alone is safe, VitC in combination with AS1411-CS/rGO/Ag^+-DNA can induce the generation of more silver nanoparticles to robustly inhibit the growth of HepG2 cells (**Fig. 3c,d**). Moreover, this combination has only weak effects on L02 cells (**Fig. 3d**). Similar results were obtained *via* evaluating DNA damage. AS1411-CS/rGO/Ag^+-DNA+VitC treatment causes the longest tail in HepG2 cells, which means the highest degree of DNA damage (**Fig. 3e,f**). However, AS1411-CS/rGO/Ag^+-DNA+VitC fails to induce evident apoptosis in L02 cells due to the low

accumulation of AS1411-CS/rGO/Ag^+-DNA in these cells **(Fig. 3g,h**). This tumor cell-specific effect guarantees the safety of the treatment. Furthermore, we also measured ROS levels, since ROS are directly responsible for apoptosis and ROS levels positively correlate with the deposition of silver nanoparticles. VitC alone is unable to generate sufficient ROS-induced oxidative stress for inducing HepG2 apoptosis even though the VitC concentration reached a high level (above 8 mM) (**Fig. 3i**). Once VitC is combined with AS1411-CS/rGO/Ag^+-DNA, VitC-derived H_2O_2 reduces the internalized Ag^+ in AS1411-CS/rGO/Ag^+-DNA to produce the most silver deposits that instigate the highest ROS oxidative stress (**Fig. 3j**). This explains why AS1411-CS/rGO/Ag^+-DNA+VitC attains the highest anti-proliferation efficiency.

Next, the *in vivo* targeting and anti-tumor activities of AS1411-CS/rGO/Ag^+-DNA were explored. When mice with HepG2 xenografted tumors were administered with RS-CS/rGO/Ag^+-DNA *via* intravenous (*i.v.*) injection, the fluorescence signal in the tumor was negligible (**Fig. 4a**). In contrast, in tumor-bearing mice administered with AS1411-CS/rGO/Ag^+-DNA, the fluorescence signal in the tumor was high for up to 4 h. This can be ascribed to the targeting effect of AS1411, which delivers the SEOB system into the HepG2 tumor cells. Consistent with the *in vitro* results, high accumulation of the nanosystem favors rGO-enhanced catalytic reduction of Ag^+ by H_2O_2, which results in abundant silver deposits, and thereby significantly suppresses HepG2 tumor growth (**Fig. 4b,c**). Inspiringly, the tumors were smallest in the group treated with AS1411-CS/rGO/Ag^+-DNA+VitC. This result can be ascribed to the fact that VitC enhances the H_2O_2 supply in the tumor cells to facilitate more silver deposits, consequently resulting in the strongest inhibitory effect on HepG2 tumor growth. These results further demonstrate the feasibility of such a SEOB in unlocking the Ag^+ prodrug and facilitating intratumoral accumulation of silver nanoparticles to suppress tumor growth.

Pathological examination of tumors from AS1411-CS/rGO/Ag^+-DNA+VitC-treated mice showed some typical characteristics of apoptosis including cell shrinkage, nuclear density increase and nuclear rupture (**Fig. 4d**). TUNEL immunofluorescence staining revealed that AS1411-CS/rGO/Ag^+-DNA+VitC achieves the highest level of apoptosis (**Fig. 4e**). In particular, biological electron microscopic observation of tumor sections indicated the presence of vacuolization and tissue necrosis, which can be regarded as direct evidence to explain the tremendously suppressed tumor growth (**Fig. 4f)**.

General applicability of the SEOB system

The END aptamer has been documented to positively target HepG2 cells due to high expression of the endoglin receptor[24]. Therefore, we expected that the END-CS/rGO/Ag^+-DNA system would also inhibit HepG2 tumor growth. END-CS/rGO/Ag^+-DNA was easily obtained by referring to the synthesis procedure for AS1411-CS/rGO/Ag^+-DNA (**Fig. 2g** and Supplementary **Fig. S6**). The targeting ability of the chelated END aptamer allows more END-CS/rGO/Ag^+-DNA particles to enter HepG2 cells than RS-CS/rGO/Ag^+-DNA. Macroscopic silver deposits are produced only in HepG2 cells after adding VitC, which consequently induces massive HepG2 apoptosis (Supplementary **Figs S8 and S9**). **Video S1** clearly shows the astonishing ultra-rapid (15 s) phagocytosis of the green FITC-labeled bioreactor by HepG2 cells due to

END targeting. This was followed by silver deposit production and apoptosis (represented by red PI staining), due to the potent reduction ability of rGO and VitC-enhanced H_2O_2. Similar to AS1411-CS/rGO/Ag^+-DNA, END-CS/rGO/Ag^+-DNA fails to enter other normal cells (*e.g.*, 293T cells) with low endoglin expression, and no evident silver deposits are observed under the same conditions with HepG2 treatment (Supplementary **Fig. S8 and Video S2**). However, the anti-tumor outcome using END-CS/rGO/Ag^+-DNA is inferior to that using AS1411-CS/rGO/Ag^+-DNA in the absence or presence of VitC, probably due to differences in their accumulation. This is evidenced by the differences in membrane potential drop, cell viability, DNA damage, ROS production and *in vivo* anti-HepG2 tumor activity (**Figs 3 and 4**). Despite this, END-CS/rGO/Ag^+-DNA remains preferable to other non-targeting groups.

To further demonstrate the general applicability of the AS1411-CS/rGO/Ag^+-DNA SEOB prodrug, another xenograft tumor model (*i.e.*, human pulmonary carcinoma A549) was used. The A549 model gave identical results to the HepG2 model in terms of targeting and anti-tumor effects. In detail, AS1411-CS/rGO/Ag^+-DNA targets A549 cells much more effectively than RS-CS/rGO/Ag^+-DNA, since A549 cells also overexpress nucleolin[33] (Supplementary **Fig. S10**). Therefore, the Ag^+ pro-drug results in more silver deposits for killing A549 cells, especially in the presence of VitC, and there is no damage to normal L02 liver cells, as evidenced by flow cytometry data **(Fig. 5a**), trypan blue staining and MTT data (**Supplementary Fig. S11**). When A549 cells were treated with AS1411-CS/rGO/Ag^+-DNA+VitC *in vitro*, strong green JC-1 fluorescence was observed, together with a more evident DNA tailing phenomenon and more ROS production. These results indirectly demonstrate the applicability of the SEOB system to kill tumor cells (**Fig. 5b-f**). The *in vivo* targeting test reveals that the retention of AS1411-CS/rGO/Ag^+-DNA in A549 tumors progressively increases and reaches a peak at 48 h post-injection, while RS-CS/rGO/Ag^+-DNA fails to enter tumors (**Fig. 5g**). This observation validates the excellent targeting ability of AS1411-CS/rGO/Ag^+-DNA towards A549. Similar to the results obtained in the anti-HepG2 tumor experiment, the AS1411-CS/rGO/Ag^+-DNA prodrug performs best against A549 tumors in the presence of VitC. Tumor inhibition, tumor silver content and tumor cell apoptosis were all elevated when AS1411-CS/rGO/Ag^+-DNA was combined with VitC to enhance H_2O_2 production (**Fig. 5h-k**).

Biosafety evaluation of SEOB

The biocompatibility of the SEOB-unlocked Ag^+ prodrug remains a predominant concern for clinical translation. Herein, normal cynomolgus monkeys were used as a primate model to evaluate the safeties of AS1411- and End-CS/rGO/Ag^+-DNA. Astonishingly, histopathological examination of the main organs in cynomolgus monkeys revealed no injuries or apoptosis, which is suggestive of excellent biosafety (Supplementary **Fig. S12**). This result paves a solid path to clinical translation of the SEOB-unlocked Ag^+ prodrug.

Discussion

Based on the high catalytic activity of rGO, we constructed a tumor microenvironment-enabled *in situ* SEOB to unlock an Ag^+ prodrug to inhibit various tumors. In this system, intratumoral H_2O_2 acts as the reductant to generate silver nanoparticles and the rGO vehicle acts as the catalyst. The chelated aptamers in the prodrug-carrying bioreactors facilitated targeted uptake of the prodrug by tumor cells. This resulted in production of more silver nanoparticles, especially in combination with VitC, which is capable of supplying massive amounts of H_2O_2 in tumor cells. Consequently, the SEOB system was highly effective against HepG2 and A549 cells *in vitro* and against HepG2- and A549-derived tumors *in vivo*. The underlying mechanism is silver nanoparticle-derived apoptosis, associated with ROS-induced mitochondrial membrane potential reduction and DNA damage. The specific aptamer targeting and intratumoral silver nanoparticle production guaranteed excellent biosafety, with no damage to normal cells, since the SEOB system worked only in tumors. More significantly, there was no evident tissue damage in a primate model, which tremendously increases the clinical translation potential of the bioreactors and broadens the application field of intratumoral nanosynthetic medicine.

Declarations

Online methods

All methods and experimental details are included in the Supplementary Information.

Data availability

Additional data related to this paper is available from the corresponding author upon reasonable request.

Acknowledgement

This work was supported by the National Natural Science Foundation project (Grant Nos. 81430055, 82022033, 81771836 and 31630027); Changjiang Scholars and Innovative Research Team in University (No. IRT_15R13); Guangxi Science and Technology Base and Talent Special Project (No. AD17129003); and the Research and Development of Reproductive Medical Products of the Association of Southeast Asian Nations (ASEAN) of China (Guangxi) (No. 14251001).

Author contributions

#Y. Huang and L. Zhong contributed equally to this work. Y. Zhao, Y. Huang and K. Zhang conceived and designed this project. Y. Huang, L. Zhong, Z. Deng, P. Wu, H. Peng, Y. Zhong, L. Liu and J. He performed the experiments. Y. Huang, K. Zhang and Y. Zhao analyzed the data and wrote the manuscript. Y. Zhao and X. Liang supervised the project. Y. Huang, L. Zhong, K. Zhang, X. Liang and Y. Zhao commented on this manuscript.

Competing interests

The authors declare no competing financial interests.

Additional information

Correspondence and requests for materials should be addressed to K. Z. (zhang1986kun@126.com), L. X. (liangxj@nanoctr.cn) and Y. Z. (yongxiang_zhao@126.com).

ORCID

Kun Zhang: 0000-0002-6971-1164

Yongxiang Zhao: 0000-0003-2214-5587

Xing-Jie Liang: 0000-0002-4793-1705

References

1. Zheng, D.-W.*, et al.* Phage-guided modulation of the gut microbiota of mouse models of colorectal cancer augments their responses to chemotherapy. *Nat. Biomed. Eng.* **3**, 717-728 (2019).
2. Sung, Y.C.*, et al.* Delivery of nitric oxide with a nanocarrier promotes tumour vessel normalization and potentiates anti-cancer therapies. *Nat Nanotechnol* **14**, 1160-1169 (2019).
3. Liu, W.-L.*, et al.* Cytomembrane nanovaccines show therapeutic effects by mimicking tumor cells and antigen presenting cells. *Nat. Commun.* **10**, 3199 (2019).
4. Xu, J.S.*, et al.* Precise targeting of POLR2A as a therapeutic strategy for human triple negative breast cancer. *Nat Nanotechnol* **14**, 388-397 (2019).
5. Chen, J.*, et al.* Oxygen-self-produced nanoplatform for relieving hypoxia and breaking resistance to sonodynamic treatment of pancreatic cancer. *ACS Nano* **11**, 12849-12862 (2017).
6. Fang, Y.*, et al.* Radiofrequency-sensitive longitudinal relaxation tuning strategy enabling the visualization of radiofrequency ablation intensified by magnetic composite. *ACS Appl. Mater. Interfaces* **11**, 11251-11261 (2019).
7. Zhang, K.*, et al.* Extravascular gelation shrinkage-derived internal stress enables tumor starvation therapy with suppressed metastasis and recurrence. *Nat. Commun.* **10**, 5380 (2019).
8. Zhang, K.*, et al.* Quantum yield-engineered biocompatible probes illuminate lung tumor based on viscosity confinement-mediated antiaggregation. *Adv. Funct. Mater.* **29**, 1905124 (2019).
9. Dutta, S.*, et al.* Structure of a modular polyketide synthase. *Nature* **510**, 512-517 (2014).
10. Whicher, J.R.*, et al.* Structural rearrangements of a polyketide synthase module during its catalytic cycle. *Nature* **510**, 560-564 (2014).
11. Liu, J.*, et al.* Genetically targeted chemical assembly of functional materials in living cells, tissues, and animals. *Science* **367**, 1372-1376 (2020).

12. Yuan, Y.*, et al.* Furin-mediated intracellular self-assembly of olsalazine nanoparticles for enhanced magnetic resonance imaging and tumour therapy. *Nat. Mater.* **18**, 1376-1383 (2019).
13. de Lazaro, I. & Mooney, D.J. A nanoparticle's pathway into tumours. *Nat Mater* **19**, 486-487 (2020).
14. El Hazek, M.N., Lasheen, T.A. & Helal, A.S. Reductive leaching of manganese from low grade Sinai ore in HCl using H_2O_2 as reductant. *Hydrometallurgy.* **84**, 187-191 (2006).
15. Htet, Y., Lu, Z., Trauger, S.A. & Tennyson, A.G. Hydrogen peroxide as a hydride donor and reductant under biologically relevant conditions. *Chem. Sci.* **10**, 2025-2033 (2019).
16. Wang, G.*, et al.* Antibacterial effects of titanium embedded with silver nanoparticles based on electron-transfer-induced reactive oxygen species. *Biomaterials* **124**, 25-34 (2017).
17. Wang, Z.*, et al.* Embedding ultrasmall Ag nanoclusters in Luria-Bertani extract *via* light irradiation for enhanced antibacterial activity. *Nano Res.* **13**, 203-208 (2020).
18. Chung, C.*, et al.* Biomedical applications of graphene and graphene oxide. *Acc. Chem. Res.* **46**, 2211-2224 (2013).
19. Han, B.*, et al.* Plasmonic-assisted graphene oxide artificial muscles. *Adv. Mater.* **31**, 1806386 (2019).
20. Yoon, H.J.*, et al.* Sensitive capture of circulating tumour cells by functionalized graphene oxide nanosheets. *Nat Nanotechnol* **8**, 735-741 (2013).
21. Song, Y., Qu, K., Zhao, C., Ren, J. & Qu, X. Graphene oxide: Intrinsic peroxidase catalytic activity and its application to glucose detection. *Adv. Mater.* **22**, 2206-2210 (2010).
22. Yong, Y.-C., Yu, Y.-Y., Zhang, X. & Song, H. Highly active bidirectional electron transfer by a self-assembled electroactive reduced- graphene-oxide-hybridized biofilm. *Angew. Chem. Int. Ed.* **53**, 4480-4483 (2014).
23. Wu, X., Qjao, Y., Shi, Z., Tang, W. & Li, C.M. Hierarchically porous N-doped carbon nanotubes/reduced graphene oxide composite for promoting flavin-based interfacial electron transfer in microbial fuel cells. *ACS Appl. Mater. Interfaces* **10**, 11671-11677 (2018).
24. Huang, Y.*, et al.* PEGylated immunoliposome-loaded endoglin single-chain antibody enhances anti-tumor capacity of porcine alpha 1,3GT gene. *Biomaterials* **217**, 119231 (2019).
25. Agathocleous, M.*, et al.* Ascorbate regulates haematopoietic stem cell function and leukaemogenesis. *Nature* **549**, 476-481 (2017).
26. Cimmino, L.*, et al.* Restoration of TET2 function blocks aberrant self-renewal and leukemia progression. *Cell* **170**, 1079-1095 (2017).
27. Yun, J.*, et al.* Vitamin C selectively kills KRAS and BRAF mutant colorectal cancer cells by targeting GAPDH. *Science* **350**, 1391-1396 (2015).
28. Ma, Y.*, et al.* High-dose parenteral ascorbate enhanced chemosensitivity of ovarian cancer and reduced toxicity of chemotherapy. *Sci. Transl. Med.* **6**, 222ra218 (2014).
29. Ordonez-Moran, P., Dafflon, C., Imajo, M., Nishida, E. & Huelsken, J. HOXA5 counteracts stem cell traits by inhibiting wnt signaling in colorectal cancer. *Cancer Cell* **28**, 815-829 (2015).

30. Garrido, G., *et al.* Tumor-targeted silencing of the peptide transporter TAP induces potent antitumor immunity. *Nat. Commun.* **10**, 3773 (2019).
31. He, J., *et al.* Molecularly engineering triptolide with aptamers for high specificity and cytotoxicity for triple-negative breast cancer. *J. Am. Chem. Soc.* **142**, 2699-2703 (2020).
32. Yerneni, S.S., *et al.* Rapid on-demand extracellular vesicle augmentation with versatile oligonucleotide tethers. *ACS Nano* **13**, 10555-10565 (2019).
33. Yang, Q., *et al.* Conjugating aptamer and mitomycin C with reductant-responsive linker leading to synergistically enhanced anticancer effect. *J. Am. Chem. Soc.* **142**, 2532-2540 (2020).

Figures

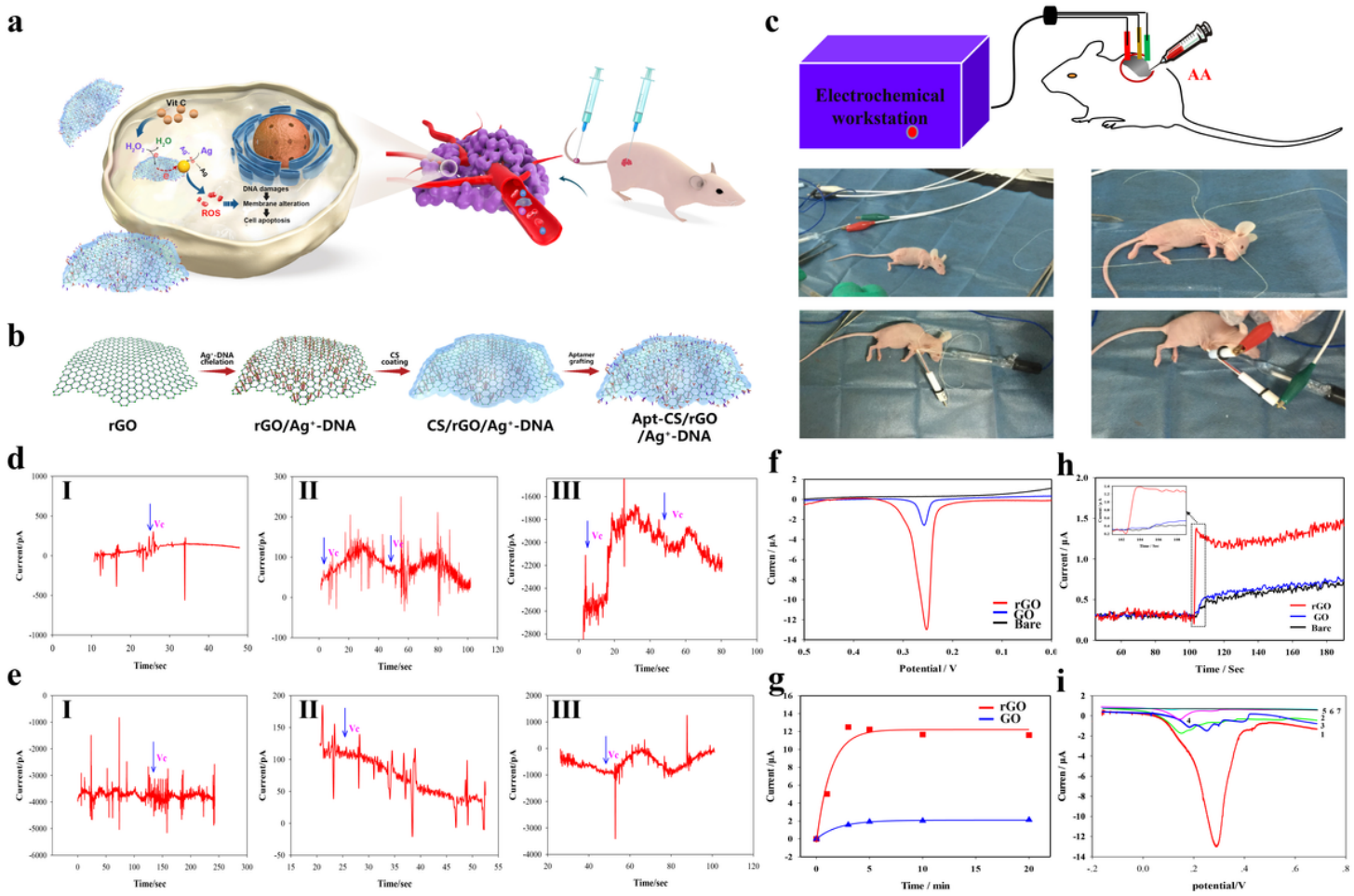

Figure 1

Clarification of the principle underlying the SEOB, and exploration of the mechanism for unlocking the Ag+ prodrug. (a) The underlying principle of the SEOB, which unlocks the Ag+ prodrug to kill tumor cells. (b) Illustration of the synthesis procedure of the Ag+-based prodrug-carrying bioreactor (i.e. Apt-CS/rGO/Ag+-DNA). (c) Schematic and real images of the electrochemical workstation for detecting intratumoral H2O2 production in situ in HepG2 tumor-bearing mice. (d) ASV signal after intravenous (i.v.)

injections of different treatments into HepG2 tumor-bearing mice or normal mice. I: 100 μL normal saline into normal mice, no signal alteration; II: 100 μL VitC (5 mM) into normal mice, slightly fluctuated response current; III: 100 μL VitC (5 mM) into HepG2 tumor-bearing mice, 800 pA current. (e) ASV signal after intratumoral (i.t.) injections of different treatments into HepG2 tumor-bearing mice or normal mice. I: 100 μL normal saline into normal mice, no signal alteration; II: 100 μL VitC (5 mM) into normal mice, 50 pA current; III: 100 μL VitC (5 mM) into HepG2 tumor-bearing mice, 1000 pA current. (f) ASV signal of rGO-catalyzed silver deposits on different electrodes; (g) Kinetic curves for silver deposits catalyzed by rGO-modified and GO-modified electrodes. (h) i-t signal response of H2O2 disproportionation catalyzed by different electrodes. The i-t curve regions of interest are magnified in the dotted box. (i) ASV tests for evaluating rGO-boosted silver deposition from free Ag+-DNA conjugates. Curves 1-7 were obtained under different conditions as follows. Curves 1-3: rGO-modified electrode, 300 μL of mixed solution including Ag+ (100 mM), H2O2 (10 mM) and DNA (50 μM, 5 μM and 0 μM, respectively), peak response signals: 40 μA, 4.5 μA and 3.5 μA, respectively; Curves 4-6: GO-modified electrode, 300 μL of mixed solution containing (curve 4, pink) 5 μM DNA-100 mM Ag+-10 mM H2O2 with 2.1 μA signal, (curve 5, black) 100 mM Ag+-10 mM H2O2 with no response signal, and (curve 6, light blue) 100 mM Ag+ with no response signal; Curve 7 (brown): bare electrode; no response signal.

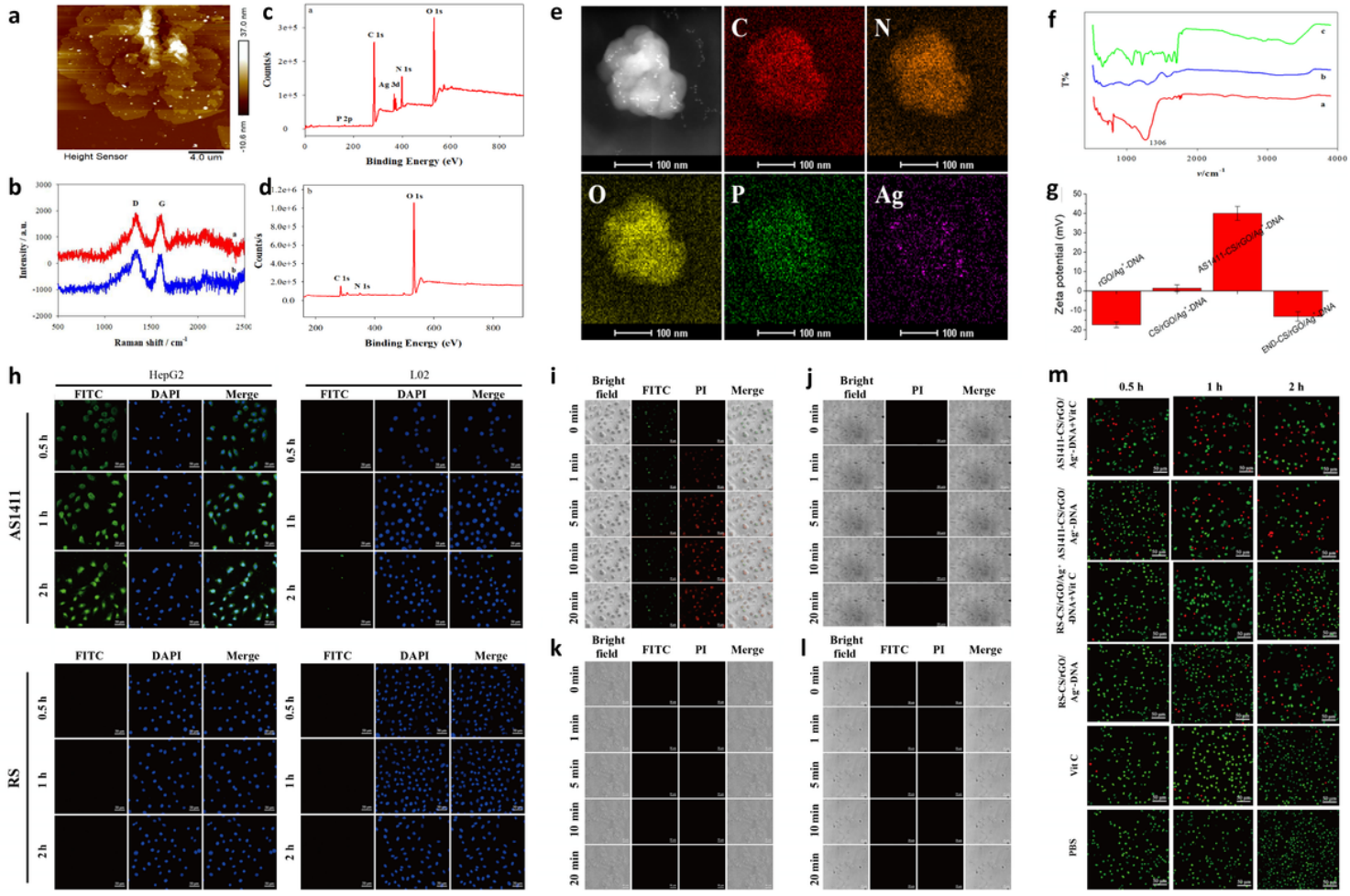

Figure 2

Evaluations of the ability of the bioreactors AS1411-CS/rGO/Ag+-DNA and END-CS/rGO/Ag+-DNA to unlock the Ag+-based prodrug. (a) Atomic force microscopy (AFM) image of AS1411-CS/rGO/Ag+-DNA; (b-d) Raman (b) and XPS spectra (c,d) of AS1411-CS/rGO/Ag+-DNA (c) and rGO (d). (e) Atom mapping images of different atoms in AS1411-CS/rGO/Ag+-DNA; (f,g) FT-IR spectra of rGO/Ag+-DNA (1), CS/rGO/Ag+-DNA (2) and AS1411-CS/rGO/Ag+-DNA (3); (g) zeta potential of AS1411-CS/rGO/Ag+-DNA and its intermediate products. (h) LCSM images of HepG2 and L02 cells (1×104) after treatments with 100 μL of 1.0 mg/mL AS1411-CS/rGO/Ag+-DNA or RS -CS/rGO/Ag+-DNA for 0.5 h, 1 h and 2 h; dose: 1 mg/ml. (i) HepG2 cells (1×104) were incubated with 100 μL of 1.0 mg/mL AS1411-CS/rGO/Ag+-DNA, then washed with PBS. 100 μL of pyridine iodide (PI) dye (1 mg/mL) was added, and the cells were treated with 10 μL of 5 mM VitC for the indicated time. (j) 100 μL of PI dye (1 mg/mL) was added into HepG2 cells (1×104), and the cells were treated with 10 μL of 5 mM VitC for the indicated time. (k) L02 cells (1×104) were incubated with 100 μL of 1.0 mg/mL AS1411-CS/rGO/Ag+-DNA, then washed with PBS. 100 μL of 1 mg/mL PI dye was added, and the cells were treated with 10 μL of 5 mM VitC for the indicated time. (l) L02 cells (1×104) were incubated with 100 μL of 1.0 mg/mL RS-CS/rGO/Ag+-DNA, then washed twice with PBS. 100 μL of PI dye (1 mg/mL) was added, followed by 10 μL of 5 mM VitC. (m) HepG2 cells (1×104) were subjected to the indicated treatments for different incubation periods (0.5 h, 1 h and 2 h). The cells were then co-stained with calcein and PI, and imaged by LCSM. Scale bar: 50 μm.

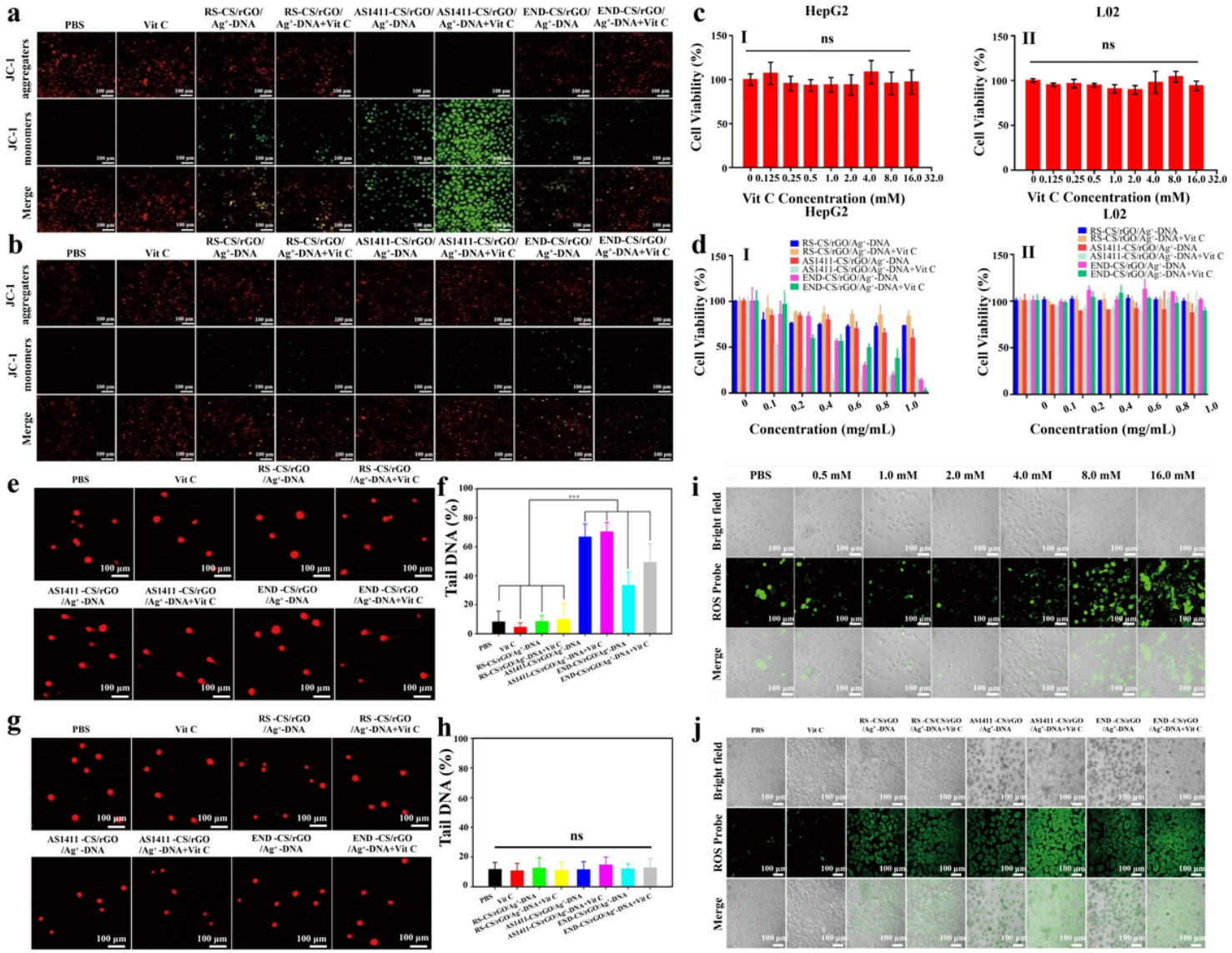

Figure 3

In vitro investigations of the effects of the SEOB-unlocked Ag+-based prodrug on membrane potential, viability, DNA damage and ROS production in cultured cells. (a,b) LCSM images of JC-1 signal produced by HepG2 (a) and L02 (b) cells (1×106) after treatment with the indicated formulations; (c) MTT data of HepG2 and L02 cells (1×104) after incubation with various concentrations of VitC. (d) MTT data of HepG2 and L02 cells (1×104) after treatment with the indicated formulations. (e-h) LCSM images and statistical analysis of DNA damage in HepG2 (e,f) and L02 (g,h) cells. The cells (1×105) were subjected to DNA staining after the indicated treatments. (i) LCMS images of ROS signal produced by HepG2 (1×106) after incubation with various concentrations of VitC. (j) LCMS images of ROS signal produced by HepG2 cells. The cells (1×106) were subjected to ROS probe staining after the indicated treatments. Data are presented as mean ± standard deviation (SD) (n=3), and statistical significance was determined by one-way ANOVA and Tukey's multiple comparisons test. n.s., P ⍰ 0.05; ***P < 0.001. Scale bar: 100 μm. Note, Apt-CS/rGO/Ag+-DNA: 100 μL, 1 mg/mL; VitC: 100 μL, 5 mM.

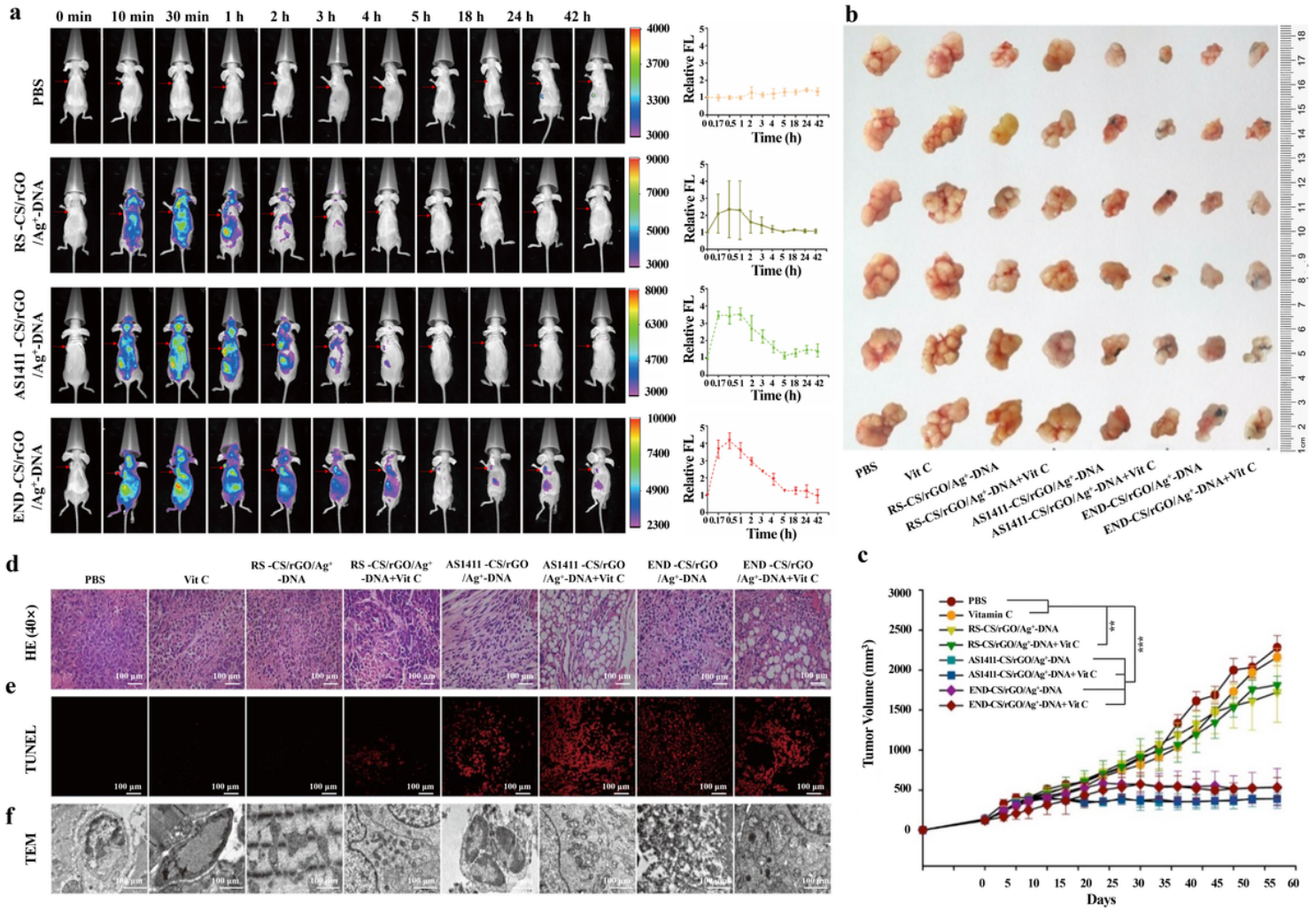

Figure 4

Evaluation of the in vivo anti-tumor effects of the SEOB on a HepG2 tumor model. (a) In vivo fluorescence imaging of HepG2 tumor-bearing nude mice to evaluate the specific targeting ability of AS1411 and END aptamers. Mice in different treatment groups were administered with the indicated formulations (sample dose: 100 μL, 1 mg/mL.). Red arrows indicate the tumor. (b) Digital photos of harvested tumors from HepG2 tumor-bearing nude mice at the end of the experimental period. Mice in different treatment groups were administered with the indicated formulations (sample dose: 100 μL, 1 mg/mL; Vit C: 100 μL, 0.1 M.). (c) Time-dependent variation profiles of HepG2 tumor volume in the different treatment groups. (d-f) H&E (d), TUNEL (e) and bio-TEM (f) pathological examinations of tumor slices from the different treatment groups at the end of the experimental period. Data are presented as mean ± standard deviation (SD) (n=6), and statistical significance was determined by one-way ANOVA and Tukey's multiple comparisons test. *P < 0.05, **P < 0.01 and ***P < 0.001. Scale bar: 100 μm.

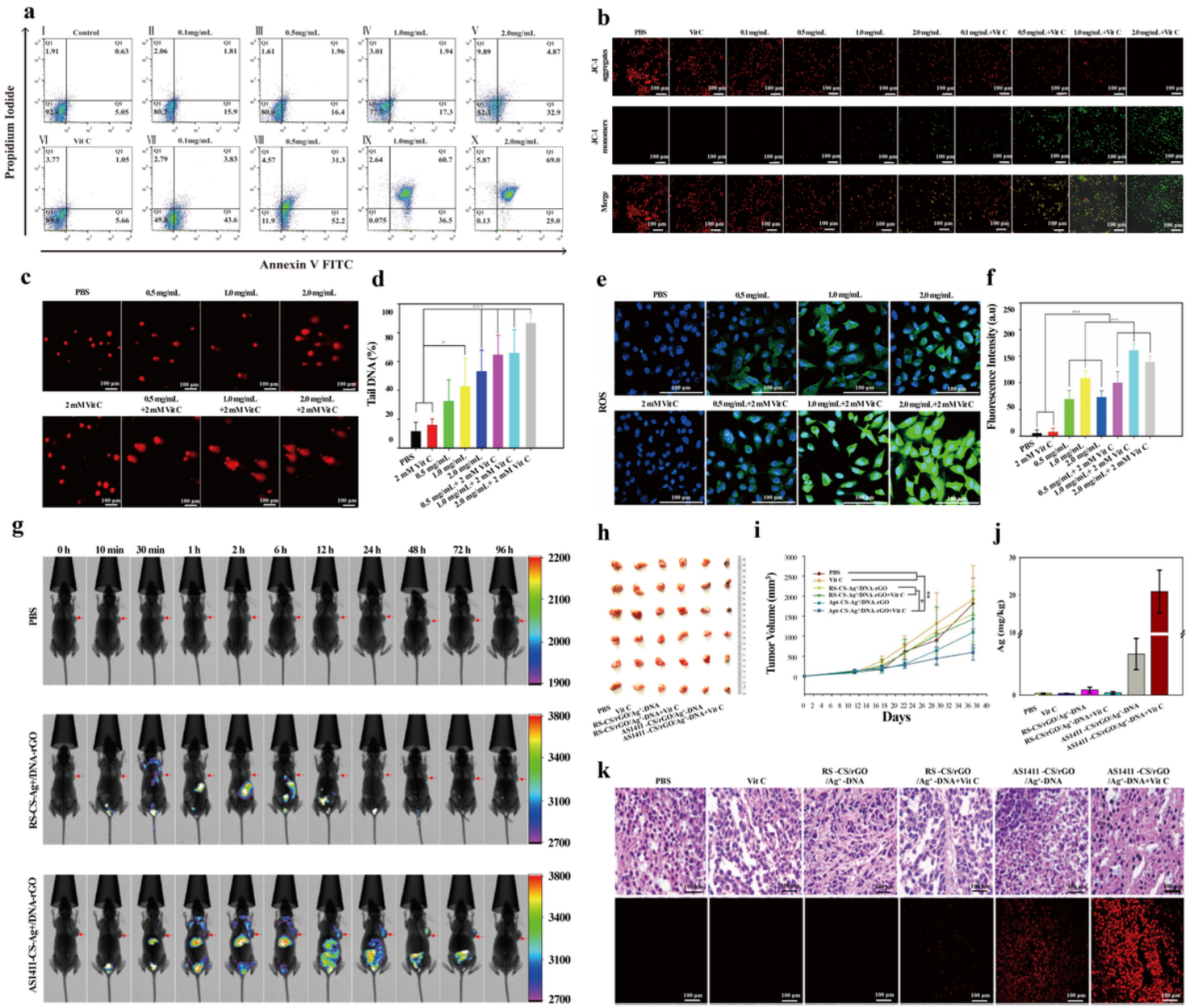

Figure 5

Evaluation of the in vivo anti-tumor effect of the SEOB system in A549 tumor-bearing mice. (a) Flow cytometry patterns of L02 (I-V) and A549 (VI-X) cells (1×106) after treatment with 100 μL of AS1411-CS/rGO-Ag+-DNA (1.0 mg/mL) and various VitC concentrations (i.e., 0 mg/mL, 0.1 mg/mL, 0.5 mg/mL, 1.0 mg/mL, 2.0 mg/mL). (b) LCSM images of the JC-1 signal produced by A549 cells (1×106). After treatment with the indicated formulations, cells were stained with JC-1 to track the variation in mitochondrial membrane potential. (c) LCSM images and statistical analysis of DNA damage in A549 cells (1×105). Cellular DNA was stained following the indicated treatments. (e,f) CLSM images (e) and statistical analysis (f) of ROS levels in A549 cells. The cells (1×106) were stained with the ROS probe following the indicated treatments. (g) In vivo fluorescence images of A549 tumor-bearing mice after i.v. injections (100 μL) of different samples, i.e., PBS, Cy5-labeled RS-CS/rGO/Ag+-DNA (1.0 mg/mL) and

AS1411-CS/rGO/Ag+-DNA (1.0 mg/mL). Red arrows indicate the tumor. (h) Digital photos of isolated tumors from A549 tumor-bearing mice in the different treatment groups at the end of the experimental period (sample dose: 100 μL, 1 mg/mL; Vit C: 100 μL, 0.1 M); (i) Volume variation profiles over time of tumors from A549 tumor-bearing mice in the different treatment groups; (j) Ag content in isolated tumors from A549 tumor-bearing mice in different treatment groups at the end of the experimental period. The Ag content was determined via ICP-MS. (k) Pathological examinations of A549 tumor slices from the different treatment groups after H&E immunochemical and TUNEL immunofluorescence staining. Data are presented as mean ± standard deviation (SD) (n=6), and statistical significance was determined by one-way ANOVA and Tukey's multiple comparisons test. *P < 0.05, **P < 0.01 and ***P < 0.001. Scale bar: 100 μm.

Supplementary Files

This is a list of supplementary files associated with this preprint. Click to download.

- SupplementaryInformation.doc
- VideoS1.mp4
- VideoS2.mp4